IEEE Access
Multidisciplinary | Rapid Review | Open Access Journal

Received July 29, 2020, accepted August 3, 2020, date of publication August 6, 2020, date of current version August 19, 2020.

Digital Object Identifier 10.1109/ACCESS.2020.3014718

Analytical Modeling for Optimal Rotor Shape to Design Highly Efficient Line-Start Permanent Magnet Synchronous Motor

ABDUL WAHEED AND JONG-SUK RO, (Member, IEEE)
School of Electrical and Electronics Engineering, Chung-Ang University, Seoul 06974, South Korea

Corresponding author: Jong-Suk Ro (jongsukro@gmail.com)

This work was supported in part by the National Research Foundation of Korea through the Basic Science Research Program funded by the Ministry of Education under Grant 2016R1D1A1B01008058, and in part by the Human Resources Development of the Korea Institute of Energy Technology Evaluation and Planning (KETEP) grant funded by the Ministry of Trade, Industry and Energy of the South Korean Government, under Grant 20204030200090.

ABSTRACT In this study, an analytical technique for the rotor geometry optimization based on lumped magnetic parametric approach is used to design a two-pole, three-phase, 7.5-kW line-start permanent magnet (LSPM) synchronous motor. The permanent magnet shape substantially affects the air-gap flux density distribution, back electromotive force (EMF) as well as the copper loss, which have a great impact on the performance characteristics of the permanent magnet synchronous motors. Principal advantages involve in adjusting the rotor shape are to achieve the effective air-gap flux density and optimize the fundamental component of the back EMF with low harmonic content for minimum ripple torque. Therefore, to enhance the efficiency (η) and power factor, an optimized slot shape considering various design parameters is selected for the permanent magnet of the rotor in the prototype LSPM machine. A linear saturated lumped magnetic parametric model is developed to exhibit magnetic characteristics, and analytical equations are acquired under the open-circuit condition without considering the slotting effect for design simplicity. The influence of design variables on the air-gap flux density distribution and the flux leakage is investigated precisely using an analytical circuit model. A parametric study of the prototype model demonstrates that the steady-state performance of the LSPM motor are significantly influenced by the design variables. The inductance saliency ratio and electromagnetic torque components are carefully analyzed in terms of their effects on the load characteristics of the LSPM motor in order to determine the optimal shape of the PM slots and the magnetic flux barriers. The validity of the proposed method has been checked by evaluating the numerical solution of the analytical model using a two-dimensional finite element method.

INDEX TERMS Analytical method, air-gap flux density, FEM, lumped parametric model, parametric study, rotor design.

I. INTRODUCTION

In the 21st century, there has been a significant increase in the energy crisis due to the depletion of hydrocarbons and global warming. Consequently, the demand for measures to reduce energy consumption has also increased. Owing to these economic and environmental problems, significant research efforts have been devoted toward developing highly efficient electrical machines as an alternative to conventional machines with high energy consumption [1]–[3]. This is a result of increased customer awareness regarding low life-cycle costs, high efficiency, and compatibility as well as increased sensitivity toward environmental challenges. For instance, in industrial applications and academia, line-operated induction motors (IMs) are being replaced with line-start permanent magnet motor, owing to their high power factor (PF) and efficiency regardless of the variations in load [1], [2], [4]. LSPM motors offer a highly energy-efficient alternative to IMs, which are extensively used in industries for various applications such as low-cost electric drives, pumping systems, and compressors [1]–[3], [5], [6].

The LSPM motor is a synchronous machine in which a permanent magnet (PM) inserted in the squirrel-cage rotor produces the excitation field rather than the DC field winding,

The associate editor coordinating the review of this manuscript and approving it for publication was Atif Iqbal.

as in the case of the induction motor. The conducting bars in the squirrel-cage rotor are short-circuited using end rings, thereby enabling the LSPM motor to start with a conventional AC voltage source, without requiring an additional inverter; this leads to an effective reduction in design cost [7]–[9]. The LSPM motor operates as a synchronous motor in the steady operating condition due to the presence of magnets under the rotor bars. The LSPM motor runs at a constant speed, and the PM buried in the squirrel-cage rotor generates a reluctance torque component as a result of rotor saliency [1], [6], [8]. Therefore, this motor incorporates the benefits of the conventional interior permanent magnet (IPM) synchronous motor (high efficiency, high PF, and high torque density) and the IM (a robust construction and line-start capability). Furthermore, this type of rotor structure offers advantages such as an improved saliency ratio, a high PF, low copper loss and a good quality of protection for magnets, by realizing magnetic shielding and mechanical ruggedness [3], [5]–[7].

Exhaustive analyses of the air-gap flux density distribution and the back electromotive force (EMF) are essential as they provide key design information for optimizing the rotor structure in order to ascertain the required performance characteristics of an electrical machine [10]–[13]. The design optimization of rotor shape is critical to achieve the optimal values in no-load analysis [14]. In an electrical machine, the air-gap flux density distribution can be analyzed via two approaches: a finite element (numerical) method and an analytical method. However, the numerical method for computing the required air-gap flux density is a time-consuming, and becomes difficult for the machine designers to determine the optimum values of the machine design variables [10], [11], [15]–[17].

A lot of research has been done in the field of brushless PM synchronous machines using the conventional magnetic equivalent circuit (MEC) approach for the calculation of magnetic properties, which applied to axial flux [18], [19], flux switching [16], [21], salient-pole synchronous [22]–[24], spoke-type [25], [26] and IPM machines [12], [27]–[30] is unsuitable for optimization purposes owing to the complexities in the LSPM rotor structures and the efforts required for modeling. Moreover, the MEC-based analytical method used in [3], [7], [16], [21], [24], [27]–[31], does not account for the saturation effects in rotor bridges, resulting in high error percentages in the output results. Genetic algorithms are also considerably time-consuming because of the repetitive iteration process required to converge on the design variables for optimization [32]. Similarly, the Maxwell equations or Laplacian field equations for the analytical modeling necessitate strong mathematical knowledge and require conformal mapping to address the stator slotting effects [7], [21], [33]–[36]. Conversely, a very less attention has been paid to the LSPM motors for the optimization of complex rotor shape using linear 0-D analytical models (MEC). The general MEC models applied for the LSPM motor in [3], [7], [37], [41], offer a highly complicated nonlinear solutions and do not consider the saturation effect in the bridges due to flux leakage, a most predominant effect and may result in high percentage of error to optimize the design variables for an effective rotor shape. It is also significantly challenging to directly apply the above-mentioned analytical methods to IPM-type LSPM machine in order to predict the air-gap field distribution under an open-circuit condition, because of the significant flux leakage and magnetic saturation in the bridges.

Generally, to obtain a high PF with minimal line current, an optimal size of the PM segments must be used to deliver the required flux density in order to minimize the reactive power exchanged with the power supply. The previously adopted MEC models are unsuitable for the optimization purposes in LSPM motor due to complex rotor structures and much efforts are needed for analytical modeling [3], [7], [37], [41]. Therefore, in this study, to improve the efficiency and PF of 7.5-kW LSPM motor, a linear saturated lumped parametric circuit model (LPM) is developed for the analysis of the air-gap flux density, with the aim of optimizing the design variables and realizing an effective shape for the PM slots and flux barriers. To the best of author's knowledge, an improved LPM method based on the conventional MEC approach has not yet been proposed to optimize the convex-shaped rotor of the LSPM motor including flux leakage for the analytical modeling [10], [11], [13], [15], [39], [40]. A careful investigation is performed to evaluate the effects of the rotor pole shape on the air-gap flux density distribution. This method accounts for the saturation in bridges as well as other material properties, while offering considerable simplicity and accuracy. A finite element method (FEM) is used to obtain a precise image of the magnetic flux distribution in the machine; this is crucial for determining the exact position and energy of the magnetic material and for investigating the influence of flux barrier [11], [15], [39].

In this research, a simple linear saturated 0-D analytical method (LPM) is employed to calculate the effective average air-gap flux density as a prerequisite in order to obtain the critical design parameters for maximum value of the fundamental component of back EMF with low harmonic content; this model incorporates the flux leakage through the rotor flux barriers and bridges [10]–[12], [15], [38], [40]. This procedure is much simpler than previous methods applied for the analytical modeling of LSPM motors in [3], [7], [37]. The optimized magnet slot shape and magnetization direction are critical for producing a uniform magnetic flux density in the air gap. The validity of the design optimization approach is established by comparing the results of the proposed analytical method with those of the FEM. The slot angle of the side PM segment (α_m) and the distance of the PM slot (L_P) are variables of the objective function (efficiency and PF) in the lumped magnetic parametric study of the prototype LSPM model, as shown in Fig. 1. The air-gap flux density waveform and back EMF voltages are optimized efficiently, while other performance constraints, such as start-up and synchronization capability, are considered to maximize the objective function [1], [5]–[8], [13].

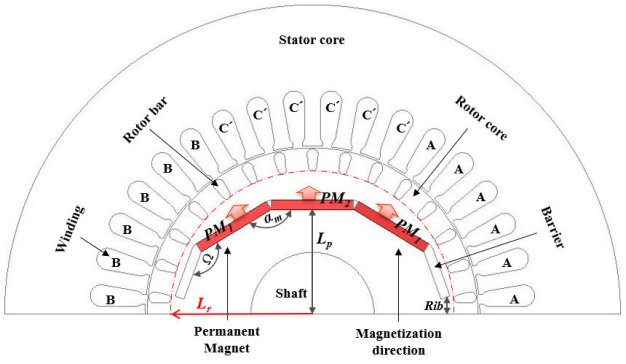

FIGURE 1. 7.5kW prototype LSPM model structure.

The rectangular shaped low-cost interior PM segments are used in the laminated rotor core to produce the effective reluctance torque due to salient structure for enhanced torque performance. The effect of inductance design on the LSPM load characteristics was also carefully investigated for determining the optimal structure of the rotor [6], [28]. Inductance saliency ratio is typically associated with total electromagnetic torque and PF. Therefore, the reluctance torque due to rotor saliency and winding excitation are the main factors for LSPM rotation in steady-state condition [4], [6]. The optimized PM slot structure was employed for the prototype LSPM motor; this structure improves efficiency, PF, and anti-demagnetizing capability at high temperatures [8], [42], [43]. The influences of magnet height (L_P) from the rotor shaft and the pole-arc to pole-pitch ratio (τ_P) in terms of slot angles were carefully investigated to analyze their impact on the output performance of the LSPM motor. These analyses help in modifying the optimized structure of the PM slot in the prototype LSPM rotor.

II. DESIGN STUDY OF THE PROTOTYPE MACHINE

A 7.5-kW LSPM motor was designed and analyzed. Figure 1 presents the three-phase, two-pole (each consisting of three magnet segments) prototype motor structure. The structure of this prototype machine comprised a rectangular-shaped PM inserted in the rotor core of a standard three-phase induction motor [5], [7], [44]. The optimal rotor with a convex-type shape has a radial magnetization direction and considerably influences the performance characteristics of the LSPM motor [13]. The squirrel-cage on the rotor is composed of aluminum, and there are 30 conducting bars, with P being the number of poles. The material of the stator core is steel (s18), and there are 36 stator slots. The rare-earth material neodymium iron boron (Nd–Fe–B), which is used as the PM, has a width of 26 mm, axial length 130 mm and its coercive force and residual flux density are $H_c = 890$ kA/m and $B_r = 1.23$T, respectively. A 7.5kW two-pole LSPM motor consists of a single-layer three phase distributed winding configuration. The number of conductors per slot are 24. The three-phase distributed winding is connected in Y-delta mode. This type of winding connection is necessary to tackle the high starting current of the three-phase armature circuit in the LSPM motor [45].

The LSPM motor starts as an asynchronous machine by utilizing an induction cage rotor, and it runs as a normal synchronous motor under steady-state condition. The LSPM motor has a high starting current owing to the high braking and pulsating torque component generated by the PM [2], [6], [46]. The PM slot shape and rotor bars are designed such that the starting current must be as low as possible to avoid demagnetization phenomena caused by the reverse magnetomotive force (MMF) produced at high temperatures. An analysis of the demagnetization characteristics is important to identify the reliable rotor design. The effective rotor structure with an optimized PM slot enhances the anti-demagnetizing capability by providing magnetic shielding through the eddy currents in the rotor bar of the LSPM motor, under the transient-state conditions [3], [5], [8], [43].

The design modification involves the position of the magnet from the rotor shaft, length and width of the magnets, gap between rotor slots and bars, size and shape of flux barriers, and length of the bridges. As the PMs provide the primary excitation field, magnetization windings are not required. This leads to an increase in the PF under the full-load condition and reduces copper loss [2], [3], [14]. The design of the flux barriers, slot angle of side PM segments, and distance from the center of the shaft are optimized to achieve the highest flux linkage for the stator winding with the minimum phase current. The linear lumped magnetic model helps to optimize the PM slot angle (α_m) and precise position (L_P) of the magnets inside the rotor core. Thus, FEM is an inevitable choice to analyze the optimized rotor structure of the LSPM motor, in order to acquire a high efficiency and PF. The shape of the flux barriers and magnet segments are optimized by calculating the air-gap flux density (B_g), back EMF, L_d and L_q inductances, efficiency (η), PF, and electromagnetic torque (T_e) at the rated speed (n_r). The primary design specifications of the prototype LSPM motor are summarized in Table 1.

TABLE 1. Design specifications of the prototype LSPM model.

Symbol	Quantity	Value
-	Phase	3
P	Poles	2
T_r	Rated torque [N m]	19.9
n_r	Rated speed [rpm]	3600
f	Frequency [Hz]	60
D_{so}	Stator outer diameter [mm]	195
D_{ro}	Rotor outer diameter [mm]	105
L_{stk}	Stack length [mm]	130
-	Number of stator slots	36
-	Number of rotor bars	30
-	Rotor bar material	aluminum
PM	Magnet material	Nd–Fe–b
-	Br at 100 °C [T]	1.23
-	Hc at 100 °C [kA/m]	890
T_m	PM thickness [mm]	3

The process of designing the LSPM motor is focused on the rotor structure because the volume of the air gap and the stator windings (D^2L) are similar to those of a conventional three-phase induction motor [5], [6], [42]. Throughout the design process, the same stator core, frame size, and winding configurations of the IM are applied to reduce development time and cost [3], [5], [8], [45]. This research focused solely on the rotor structure to obtain the required optimal specifications for pumping system. The rotor can feature different configurations depending on the shapes, sizes, materials, and position of the inserted PMs, all of which considerably influence the performance of the LSPM motor [3], [6], [14]. This research focuses on the improvement of the efficiency, PF, and armature current of the LSPM, based on the PM position and slot angles in terms of the pole-arc to pole-pitch ratio (τ_P). The detailed investigation of the rotor shape based on proposed analytical model with mathematical expressions and the impact of the design variables is described in the following sections.

III. PROPOSED ANALYTICAL MODELING FOR THE LSPM MOTOR

A. LUMPED PARAMETRIC MODEL

The analytical method is essential to minimize the time required for calculation, particularly during the design optimization process. First, the basic concepts of the IPM motor were studied in detail, and the linear saturated lumped parametric circuit model (LPM) of the LSPM motor was developed using an analytical method, while accounting for the magnetic saturation in different regions [10], [12], [38], [40]. A 0-D analytical method based LPM can be extracted for fixed rotor position to replicate the various rotor rotations which involve iterative computation process like FEM for modeling and the optimization of electromagnetic devices [38]. The improved saturated LPM provides an excellent means to understand the electromagnetic modeling in order to optimize the complex rotor structure by using effective design parameters, their influence during the advance stage, and the corresponding effect of bridges, rotor bars. This design method is formulated to obtain an optimal rotor shape for LSPM motor with minimum flux leakage, in order to effectively improve magnetic loading [10]–[12], [31], [39].

The LPM adopted for an analytical modeling can only consider one magnetization direction of the PM, particularly either in parallel or tangential direction [47]. Although, it is a radial flux type LSPM motor and the most predominant component of air-gap flux density is radial one rather than tangential component [48]. The tangential component of the air-gap flux density will be dominant, if a large or variable air gap length exists as in the case of axial flux [18]–[20], flux switching [16], [21], salient-pole PM machines [22]–[24], spoke-type [25], [26], and PM linear synchronous [48]–[50]. Therefore, the LPM approach proposed for the convex-shaped LSPM rotor considers only the most dominant radial component of the air-gap flux density in the 0-D analytical model [13], [47], [48].

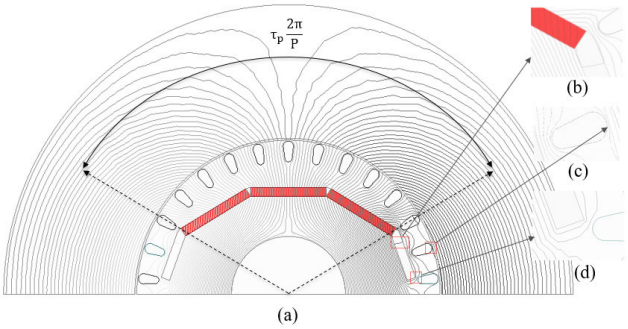

FIGURE 2. Distribution of flux lines in the prototype LSPM model.

The LPM model comprises on the magnetic flux sources, reluctances, and MMF sources equivalent to the resistive electric circuits. The accuracy of the adopted optimization method depends on the discretization of the prototype model. A 36-slot, two-pole LSPM motor with a convex-shaped PM rotor, as shown in Fig. 2(a), is modeled to validate the proposed analytical method. In this study, the improved linear lumped circuit model is employed to optimize the rotor structure for predicting machine performance parameters, such as efficiency, PF, and torque, by using the air-gap flux density predicting machine performance parameters, and dq-axis inductances. Using this 0-D method, the influence of the design variables on the average air-gap flux density can be examined thoroughly. For analyzing the magnetic field characteristics of the LSPM using LPM, the following assumptions are required [10]–[12], [15], [38], [48]–[50]:

1. The permeability of the iron core is infinite.
2. End winding effects are also neglected.
3. Eddy current reaction in no-load condition is ignored.
4. Magnetic saturation effect is excluded (except in bridge, where given as a constant saturated flux density $B_{sat.}$).
5. Slotting effects are ignored only to simplify the analysis for the calculation of air-gap flux density distribution.
6. Irreversible demagnetization of the magnet is neglected.

The LPM model is used to refine the complex rotor structure of the LSPM motor by analytically calculating the effective fundamental component of the magnetic flux density in the air gap, and improve the back EMF waveform to control the deteriorating harmonic contents [10], [11], [40]. Furthermore, FEM is used to verify the output results of the proposed analytical model, for determining the optimal shape of the PM slot. Figure 2 depicts the flux lines distribution in the LSPM motor at no-load condition; here, a smooth stator is considered, i.e., omitting the slotting effect, to develop a simple and useful analytical model during the early design stage. There is no saturation in the stator and rotor yokes, and their permeance effect is neglected for simplicity in the analytical method. Nonetheless, the results still yield high accuracy. Non-magnetic flux barriers are inserted to avoid a magnetic short-circuit and to control the magnetization of

the poles. The lumped circuit model according to the flux lines predicted by FEM is shown in Fig. 3 [11], [15], [39].

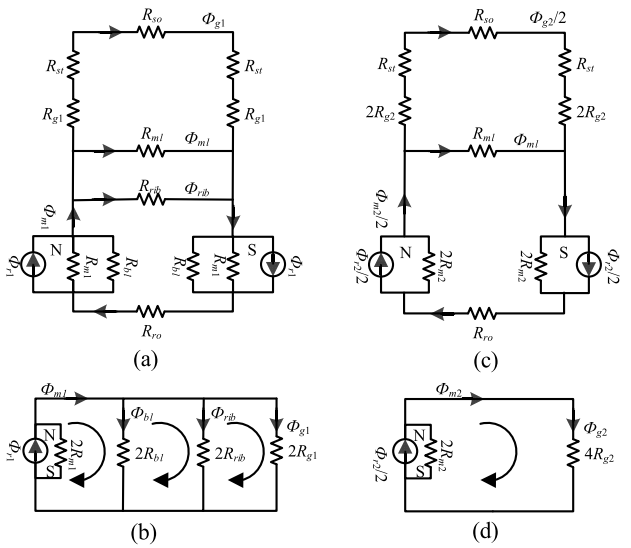

FIGURE 3. Lumped parametric circuit models (a) and (b) Models based on PM_1 (c) and (d) Models based on PM_2.

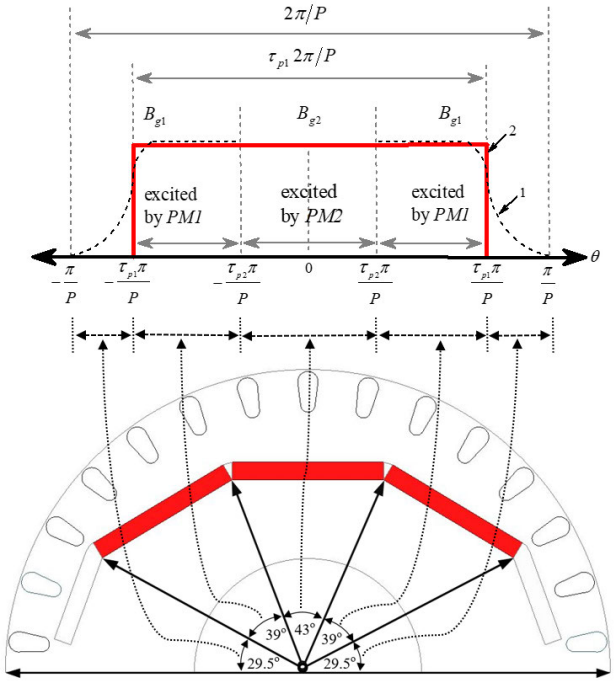

FIGURE 4. Equivalent modeling of air-gap flux density distribution.

The rotor of the LSPM motor consists of a single layer of permanent magnet segments (PM_1 and PM_2). The flux lines predicted via FEM indicate that the air-gap flux density can be segregated into two sections in a flux loop over one magnet pole pitch. Each section is excited by one full PM_1 and one half PM_2; their corresponding lumped circuit models are shown in Fig. 3(a) and (c). Therefore, the distribution of the actual air-gap flux density waveform given by curve 1 is simplified to curve 2 through LPM model in Fig. 4, depends on the fluxes produced by PM_1 and PM_2 along the circumference (θ) of the machine, where τ_P is the magnet pole-arc to pole-pitch ratio, and P is the number of poles. R_{m1} and R_{m2} are the self-reluctances of PM_1 and PM_2. The air-gap fluxes generated by the PMs over one pole pitch are ϕ_{m1} and ϕ_{m2}, and their reluctances are R_{g1} and R_{g2}, respectively. ϕ_{rib} and ϕ_{bl} are the flux leakages through *Rib* and the flux barriers and their corresponding reluctances are expressed as R_{rib} and R_{bl}, respectively. ϕ_{ml} is the PM-PM flux leakage, which is negligibly small because of the large value of *Rib* on either side of the flux barrier slots; R_{ml} is its reluctance. ϕ_{ml} is only included in the magnetic circuit model when the value of *Rib* is small. ϕ_{m1} and ϕ_{m2} are the fluxes that leave the magnet segments (PM_1 and PM_2). R_{ro}, R_{so}, and R_{st}, are the rotor and stator yoke, and stator teeth reluctances, respectively. The primary design variables for optimizing the rotor shape of LSPM motor to get an effective air-gap flux density are shown in Fig. 5. The mechanical constraints associated with the complex rotor design should be considered carefully for determining the optimal values of the design variables [11], [12], [28], [39], [40].

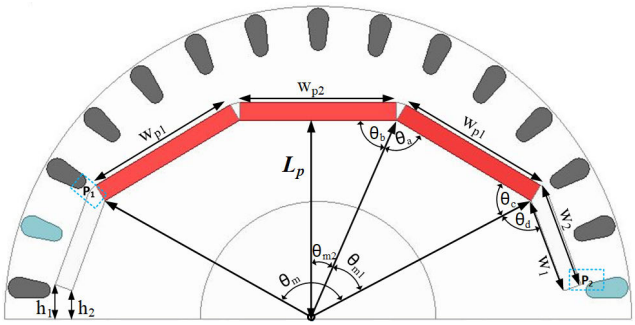

FIGURE 5. Design parameters of LSPM rotor for analytical expressions.

B. MATHEMATICAL EXPRESSIONS

For the verification of the proposed analytical approach the mathematical equations are computed, and their results are compared with FEM simulations. The LPM based analytical model of the prototype machine was designed using half of the pole arc ($\theta_m/2$) [11], [15], [39]. Thus, the output results of the proposed analytical method should indicate excellent agreement with the FEM results. The design parameters of the prototype LSPM model shown in Fig. 1 are listed in Table 2. Based on Fig. 5, the following expressions are easily obtained:

$$\phi_{r1} = B_r A_{p1} = B_r L_{stk} w_{p1}, \tag{1}$$

$$\phi_{r2} = B_r A_{p2} = B_r L_{stk} w_{p2}. \tag{2}$$

The various reluctance parameters and air-gap area can be expressed as

$$R_{g1} = \frac{g_o}{\mu_o A_{g1}}, \tag{3}$$

$$R_{g2} = \frac{g_o}{\mu_o A_{g2}}, \tag{4}$$

TABLE 2. Design parameters of LSPM machine.

B_{sat}	2.11	μ_r	1.09
τ_P	0.66	P	2
w_{p1}, w_{p2} [mm]	26	R_{sin} [mm]	53.0
w_1 [mm]	15.87	g_o [mm]	0.60
w_2 [mm]	17.71	L_P [mm]	33.0
w_{bri1} [mm]	1.52	h_1 [mm]	4.68
w_{bri2} [mm]	0.30	h_2 [mm]	4.93

$$R_{m1} = \frac{T_{m1}}{\mu_o \mu_r L_{stk} w_{p1}}, \tag{5}$$

$$R_{m2} = \frac{T_{m2}}{\mu_o \mu_r L_{stk} w_{p2}}, \tag{6}$$

$$R_{bl} = \frac{2T_{bl}}{\mu_o L_{stk}(w_1 + w_2)}, \tag{7}$$

$$R_{rib} = \frac{2T_{rib}}{\mu_o L_{stk}(h_1 + h_2)}, \tag{8}$$

$$A_g = \tau_P \frac{\pi(R_{sin} - g_o/2)}{P} L_{stk}, \tag{9}$$

where μ_r is the relative permeability of the PM, μ_0 is the permeability of air, B_r is the remanence of the magnet, L_{stk} is the stack length in axial direction, g_o is the air-gap length, w_1 and w_2 are the widths of the flux barrier slots, T_{rib} is the *Rib* thickness, h_1 and h_2 are the axial lengths of the *Rib*, R_{sin} is the inner radius of the stator core, w_{p1} and w_{p2} are the magnet widths, and T_m is the thickness of the PM [11], [15]. The thickness of each PM block used in the original LSPM model is 3 mm. The air-gap area (A_g) relies on the pole-arc to pole-pitch ratio (τ_P); it is calculated as [15], [40]

$$\tau_P = \frac{\text{pole-arc}}{\text{pole pitch}} = \frac{\theta_m}{\theta_P}. \tag{10}$$

Based on the shape of the rotor in the LSPM motor, the pole-arc angle (θ_m) acquired using PM segments in the pole to determine the effective air-gap area is expressed as [11]

$$\frac{\theta_m}{2} = (\theta_{m1} + \theta_{m2}), \tag{11}$$

$$\alpha_m = \theta_a + \theta_b, \quad \Omega = \theta_c + \theta_d, \tag{12}$$

$$A_g = A_{g1} + A_{g2}. \tag{13}$$

Here, θ_{m1} and θ_{m2} are the pole arcs of PM_1 and PM_2, respectively. Hence, A_{g1} and A_{g2} are expressed as [11], [15]

$$A_{g1} = (\frac{\theta_{m1}}{\theta_P}) \frac{2\pi(R_{in} - g_o/2)}{P} L_{stk}, \tag{14}$$

$$A_{g2} = (\frac{\theta_{m2}}{\theta_P}) \frac{2\pi(R_{in} - g_o/2)}{P} L_{stk}. \tag{15}$$

Thus, the values of θ_{m1} and θ_{m2} are

$$\theta_{m1} = \sin^{-1} \times \left[\frac{R_{ro} - (L_r + w_{p1} + w_{rb} + w_{bri1} + w_{bri2}) \sin\theta_c / R_{ro} -}{\left(L_r + \sqrt{(L_P)^2 + (w_{p2}/2)^2} + w_{rb} + w_{bri1} + w_{bri2}\right)} \right], \tag{16}$$

$$\theta_{m2} = \tan^{-1} \left[\frac{R_{ro} - (L_r + w_{p2}/2 + w_{rb} + w_{bri1} + w_{bri2})}{R_{ro} - (L_r + L_P + w_{rb} + w_{bri1} + w_{bri2})} \right]. \tag{17}$$

Here, L_r is the length from the center of the shaft to the rotor bar; w_{bri1} and w_{bri2} are the widths of the bridges between squirrel-cage bars and the rotor outer radius, at P_2 respectively, as shown in Fig. 2(c); R_{ro} is the rotor core outer radius; and w_{rb} is length of the rotor bar. Based on Fig. 5, the expression for L_P can be determined as

$$L_P = [R_{ro} - (L_r + w_{rb} + w_{bri1} + w_{bri2})] - \left[R_{ro} - \left(L_r + w_{p2} + w_{rb} + w_{bri1} + w_{bri2}\right)\right] \times \tan(\alpha_m - \theta_a). \tag{18}$$

The high saturation through the bridges makes the *Rib* a nonlinear region in the rotor. Therefore, the flux leakage in the bridges can be estimated as [10], [11]

$$\phi_{bri} \approx B_{sat} A_{bri}, \tag{19}$$

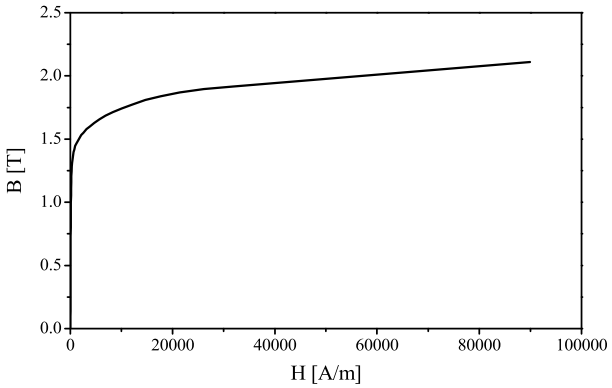

FIGURE 6. B–H curve of s18 used for lamination.

where $A_{bri} = bL_{stk}$ indicates the area of the bridge, b is the width of the bridge, and B_{sat} is the B–H curve of the steel core used for lamination, as shown in Fig. 6; here $B_{sat} = 2.11$T. Under the no-load condition, the bridges in IPM-type LSPM motor are highly saturated because of various loading conditions [14], [17], [28], [41] and the output results of the adopted LPM is still admissible, as will be explained later. By applying Kirchhoff's law to the simplified equivalent circuit of PM_1 in Fig. 3(b), the equations are obtained as:

$$R_m = \frac{2R_{m1}}{1 + \alpha + \beta}, \tag{20}$$

where

$$\alpha = \frac{R_{m1}}{R_{bl}}, \tag{21}$$

$$\beta = \frac{R_{m1}}{R_{rib}}, \tag{22}$$

$$\gamma = \frac{R_{g1}}{R_{m1}}. \tag{23}$$

The simplified equivalent circuits of PM_1 and PM_2 are used to derive the air-gap fluxes shown in Figs. 3(b) and 3(d), as follows:

$$\phi_{g1} = \frac{\phi_{r1}}{1+\gamma\,(1+\alpha+\beta)}, \tag{24}$$

$$\phi_{g2} = \frac{R_{m2}\phi_{r2}}{\left(R_{m2}+R_{g2}\right)}. \tag{25}$$

Therefore, the air-gap flux densities produced by PM_1 and PM_2 are obtained by substituting (15) and (16), and (24) and (25) in (1) and (2), respectively:

$$B_{g1} = \frac{\phi_{g1}}{A_{g1}} = \frac{B_{r1}A_{m1}}{A_{g1}\left[1+\gamma(1+\alpha+\beta)\right]}, \tag{26}$$

$$B_{g2} = \frac{\phi_{g2}}{A_{g2}} = \frac{B_{r2}A_{m2}R_{m2}}{A_{g2}\left(R_{m2}+R_{g2}\right)}. \tag{27}$$

The flux leakage of PM_1 to PM_2 is negligible and can be ignored. The PM_2 flux leakage is expressed as φ_{m2}. The flux leakages through the bridges, flux barriers, and the *Rib* only originate from PM_1 and are calculated as [11], [39]

$$\phi_{m1} = \frac{\gamma\phi_{r1}}{1+\gamma\,(1+\alpha+\beta)}, \tag{28}$$

$$\phi_{m2} = \frac{R_{g2}\phi_{r2}}{R_{g2}+R_{m2}}, \tag{29}$$

$$\phi_{bl} = \frac{\left(R_{g1}/R_{bl}\right)\phi_{r1}}{1+\gamma\,(1+\alpha+\beta)}, \tag{30}$$

$$\phi_{rib} = \frac{\left(R_{g1}/R_{rib}\right)\phi_{r1}}{1+\gamma\,(1+\alpha+\beta)}. \tag{31}$$

The equivalent model of flux distribution in Fig. 4 predict the average air-gap flux density waveform with the help of analytical model is remarkably similar to FEM results. Consequently, they are assumed to be equal to each other:

$$B_{g1} \approx B_{g2} = B_g. \tag{32}$$

Therefore, the final expression according to (L_P, α_m) for the analytical air-gap flux density can be written as follows:

$$B_g(L_P,\alpha_m) = \frac{B_{r1}A_{m1}}{A_{g1}\left[1+\gamma(1+\alpha+\beta)\right]} \approx \frac{B_{r2}A_{m2}R_{m2}}{A_{g2}\left(R_{m2}+R_{g2}\right)}. \tag{33}$$

The design parameters with their optimized values used for the prototype LSPM motor are listed in Table 2. Fig. 7 shows a comparison of the results of analytical method and those of the FEM analysis. Table 3 presents a further comparison of the analytical and FEM simulation results estimated by varying the values of τ_P, L_P, w_{p1}, w_{p2}, *Rib*, w_{bri1}, and w_{bri2}.

C. RESULTS AND VALIDATION

After designing the lumped parametric magnetic circuit, the mathematical expressions of the prototype 7.5-kW LSPM motor were derived. The analytical results are compared with the FEM simulations under open-circuit condition. The FEM simulations and analytical results calculated in the middle of the air gap were found to be considerably similar, as shown in Fig. 7. The differences between analytical outcomes of B_{g1} and B_{g2} (Table 3) are due to the increased leakage flux from PM_1 in the *Rib* and bridges (w_{bri1} and w_{bri2}) and the self-leakage through flux barriers; these cause variations in the magnetic saturation level under distinct loading conditions. Moreover, the FEM reveals the fluctuations in the air-gap flux density. The rotor saliency includes these fluctuations in the waveform of B_g because stator slot opening generated additional harmonics in the rotor pole [11]–[15], [51]. As the LPM approach employed for analytical modeling does not account for stator slotting effects, saturation in the core yokes, and fringing effect of the flux lines, the air-gap fluxes obtained are higher than those obtained via the FEM [11], [15], [39], [40].

In this article, the output results are calculated with computer having a 16-GB RAM and TM i5-7500 Processor. The LSPM motor under investigation through FEM has maximum size of the mesh length, time step and stop time for one complete electrical rotation are 2.95 mm, 0.5 msec and 16.7msec, respectively. The validity of the proposed analytical method

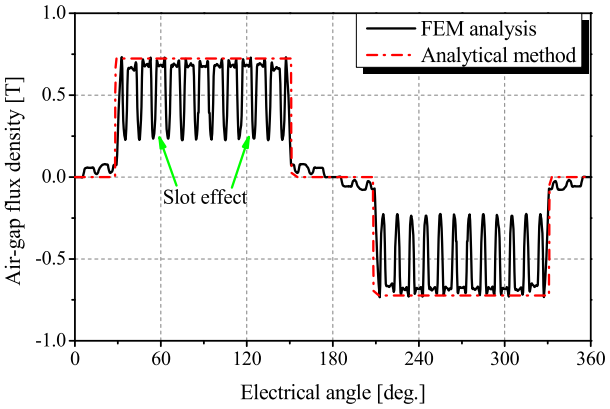

FIGURE 7. Comparative analysis of air-gap flux density distribution in the center of air gap under open-circuit condition.

TABLE 3. Comparison of analytical and FEM results.

Parameter		B_g (T) FEM (B_g)	Analytical (LPM) (B_{g1})	Analytical (LPM) (B_{g2})	Error (%) B_{g1}	Error (%) B_{g2}
τ_p	0.60	0.6698	0.6788	0.6837	1.34	2.08
	0.66	0.7231	0.7019	0.7446	2.93	2.97
	0.70	0.6369	0.6451	0.6508	1.28	2.18
L_P [mm]	30	0.6977	0.6901	0.7143	1.09	2.38
	33	0.7231	0.7019	0.7446	2.93	2.97
	36	0.8183	0.8268	0.8394	1.04	2.58
w_{p1} = w_{p2} [mm]	24	0.6689	0.6577	0.6778	1.67	1.33
	26	0.7231	0.7019	0.7446	2.93	2.97
	28	0.7621	0.7785	0.7817	2.15	2.57
Rib [mm]	2.403	0.7567	0.7463	0.7692	1.37	1.65
	4.805	0.7231	0.7019	0.7446	2.93	2.97
	7.208	0.6876	0.6759	0.6986	1.70	1.59
w_{bri1} [mm]	0.782	0.7743	0.7863	0.7928	1.55	2.39
	1.523	0.7231	0.7019	0.7446	2.93	2.97
	3.628	0.6794	0.6632	0.6912	2.39	1.74
w_{bri2} [mm]	0.2	0.7427	0.7518	0.7608	1.23	2.44
	0.3	0.7231	0.7019	0.7446	2.93	2.97
	0.4	0.7298	0.7168	0.7388	1.78	1.23

is established by comparing the LPM results with those acquired from FEM. Therefore, to determine the percentage error for better performance, the design parameters (Table 2) were varied to investigate their influence on the air-gap flux density for an optimal rotor shape. Table 3 presents a comparison of the output results of the air-gap flux density distributions; all the errors appear to be within $\leq 3\%$. This demonstrates the high accuracy level is achieved by using the proposed linear saturated LPM approach to design LSPM motors in a short time period.

The air-gap flux density is proportional to synchronous torque produced in an electrical machine. Hence, to obtain a high synchronous torque performance, the characteristics of the effective air-gap flux density distribution should be considered during the optimization process [13], [14]. This analytical method is expected to assist in achieving an optimal rotor structure for a given design objective function. This method is considerably simpler than the FEM approach, and it helps to improve the saliency ratio, efficiency, PF, and rated current of the three-phase armature winding.

IV. DESIGN VARIABLES BASED PARAMETRIC STUDY

In the parametric study, the influence of design variables on the output characteristics of the LSPM motor under no-load (average air-gap flux density, fundamental component of back EMF) and full-load conditions (total electromagnetic torque, efficiency, and PF) are investigated in detail. To maximize the objective function, it is important to improve the fundamental component of back EMF with minimal higher order harmonics. The waveform of back EMF is directly correlated with the air-gap flux density and armature winding pattern [7], [13], [14], [51]. Therefore, the developed LPM based on the local best design variables facilitates to calculate the effective air-gap flux density as well as the back EMF; this is one of the crucial steps in design optimization, and the proposed method yields more convenient results than the FEM analysis [7], [17], [21]. Several variables can be used to define the geometry of the prototype LSPM model; however, in this study, the three main design variables were fixed in order to optimize the rotor shape and achieve the most robust structure, without mechanical failure under high-speed operation. The experimental ranges of these variables are listed in Table 4.

TABLE 4. Design variables for parametric study of LSPM motor.

Design variable	Item of design	Experimental range	Unit
L_P	Length from shaft center to PM slot	28 ~ 36	mm
α_m	Slot angle of side PM segment	140 ~ 154	[deg.]
Rib	Air duct gap	2 ~ 10	mm

When evaluating the design of the LSPM motor, the shape of the bridges is the most dominant factor from air-gap flux density and mechanical point of view, to construct an effective and robust rotor structure and achieve the target specifications [17], [52]. During the design procedure, the analytical method can be used to improve the generated flux of the magnets with an optimized slot shape by reducing flux leakage and magnifying the magnet short-circuit reluctance path. Moreover, flux barriers are added in the rotor back iron to avoid magnetic short-circuit. A predefined flow of PM flux is employed to realize the required air-gap flux density. Using this method, the volume of the magnets can be reduced, thereby decreasing the overall cost of the motor; this makes the LSPM motor a viable alternative to conventional induction motors used in industrial applications. The LSPM machine combines attributes of IMs and IPM synchronous motors; however, the design and full-load operation of the LSPM motor are significantly complicated owing to this hybrid combination of synchronous and asynchronous motors [1], [5], [14], [39], [40]. The LSPM motor functions as a PM synchronous machine at synchronous speeds; theoretically, there is no current in the rotor, and the primary excitation field is provided though the magnet. This reduces the armature current required to produce magnetization under the steady-state condition. Such a reduction in armature current leads to lower copper losses and further improves both motor efficiency and the PF [2], [5], [8]. To determine the optimal values of the slot angle and the PM position for an effective back EMF, the following fundamental equation can be used:

$$\text{input voltage} = \text{back EMF} + \text{voltage drop}. \tag{34}$$

From (34), it is deduced that, with an increase in back EMF, the steady-state performance improves significantly. The back EMF and the air-gap flux density values can be increased by minimizing the leakage flux through the *Rib* and bridges (w_{bri1} and w_{bri2}); furthermore, the flux linkage to the armature winding can be improved by increasing the PM position (L_P) at the optimized value of the slot angle (α_m). The power factor and efficiency are expressed as

$$\begin{aligned} \text{PF} = \cos(\varphi) &= \cos\left[\tan^{-1}\left(\frac{\frac{L_d}{L_q}\frac{i_d}{i_q} + \frac{i_q}{i_d}}{\frac{L_d}{L_q} - 1}\right)\right] \\ &= (\xi - 1)\sqrt{\frac{\sin(2\alpha)}{2(\tan\theta + \xi^2 \cot\alpha)}}, \end{aligned} \tag{35}$$

$$\eta = \frac{P_{out}}{P_{out} + P_{loss}} = \left(1 + \frac{1}{\frac{\omega}{3.R_{th}} \cdot \left(\frac{T_e}{I^2}\right)}\right)^{-1}, \tag{36}$$

where i_d and i_q are the components of the armature winding current; L_d and L_q are the d- and q-axis inductances, respectively; ξ is the saliency ratio; I is the line current; T_e is the total electromagnetic torque; R_{th} is the total phase resistance; $P_{loss} = 3R_{th}I^2$; ω_r is the rotor angular speed of rotation; and η is the efficiency of the LSPM motor. The prototype model of the LSPM motor employing the variables used for the parametric study is illustrated in Fig. 1. The distance from

the shaft to the PM slot is L_P, the slot angle of the side PM segment is α_m, and the air duct gap is denoted as *Rib*. These design variables (α_m, L_P, and *Rib*) all depend on each other, and their influence on the optimization of the rotor shape and performance is discussed in this section.

A. SLOT ANGLE (α_m)

The analytical design method can be used to improve the performance characteristics of the prototype LSPM motor by effectively optimizing the slot angle (α_m) of the side PM segment and the PM position (L_P) inside the rotor core structure. Both L_P and *Rib* are decreased with an increase in the slot angle (α_m) of the side PM segment. The PM slot angle (α_m) is inversely proportional to pole-arc angle (θ_m). Thus, the greater the slot angle, the smaller is the pole-arc (θ_m) angle and the pole-arc to pole-pitch ratio (τ_p). Therefore, a higher value of the slot angle decreases L_P at a fixed width of the PM segments and degrades the performance characteristics of the LSPM motor, because of the high magnetic loading with additional flux leakage. The slot angle (α_m) can only increase when the fixed width of the magnet segments (w_{p1} and w_{p2}) used in the prototype model is reduced, as shown in Fig. 5; however, in this case, the high flux leakage results in low back EMF. If the volumes of the magnet segments are considered equal and the slot angle increases, the angle (Ω) between the PM slot and the flux barrier slot, as shown in Fig. 1, decreases. As a result, the pole-arc angle of the magnet and the overall pole-arc to pole-pitch ratio are reduced. When the slot angle (α_m) reaches to an optimized limit at a certain value of L_P, an effective pole-arc to pole-pitch ratio (τ_p) is obtained with good quality air-gap magnetic flux density (B_g). The optimized value of the slot angle, as compared to the pole-arc to pole-pitch ratio, is determined to ensure excellent electromagnetic performance of the prototype LSPM motor model.

Flux barrier slots featuring sizes equal to that of the PM slot are placed at the end of the side PM segments at a certain angle (Ω), while considering the mechanical limitations as given in Fig. 5. Flux barriers are introduced at the end of the PM slots to reduce the flux leakage. The impact of the reduced leakage flux on the back EMF at different slot angles is depicted in Fig. 8. At a fixed PM position (33 mm), a slot angle of 149° yields a reasonable value for the fundamental component of the induced voltage, thereby satisfying the required specifications with minimum third, fifth and seventh harmonics, unlike other slot angles. Once an appropriate path is constructed for linking the air-gap flux with the stator three-phase winding, the back EMF improves significantly.

These findings reveal the impact of taking the flux barriers at the end of the optimal PM slot shape in order to reduce flux leakage at the rotor core. The magnetic loading is decreased due to unsaturated core and has a positive effect on the armature winding current. Thus, the overall performance of the LSPM motor, including efficiency and PF, improves significantly [12], [39], [52]. The slot angle described in terms of the pole-arc to pole-pitch ratio (τ_p), as shown in Fig. 9, are used to calculate the steady-state performance characteristics

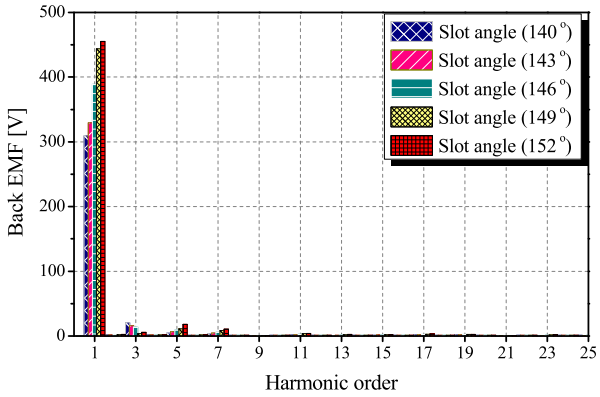

FIGURE 8. Back EMF harmonic analysis at different slot angles (α_m).

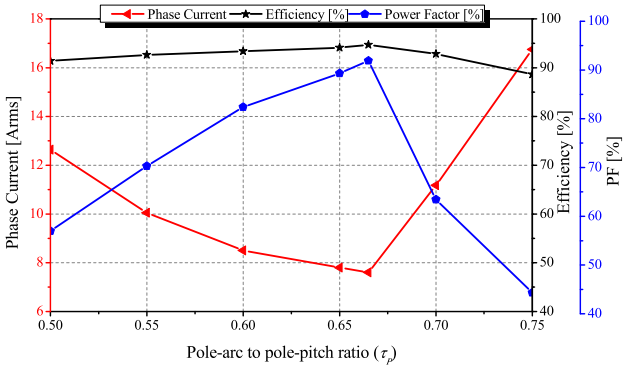

FIGURE 9. Steady-state analysis at pole-arc to pole-pitch ratio (τ_p).

of the LSPM motor. From Fig. 9, it is evident that, at the τ_p value of (0.66), high values of the efficiency (94.7%) and PF (91.9%) are achieved with a low-rated current (7.60 A_{rms}) and low copper loss (139.6 W), as compared to other pole-arc to pole-pitch ratios. This value of τ_p (0.66) is achieved when a slot angle of 149° is selected.

The slot angle (α_m) has a great influence on the linkage between the PM flux and the armature winding as well as the induced voltage. If the flux leakage is high, the rotor core is saturated to a greater extent, resulting in high magnetic loading under the steady-state operating condition. Hence, high three-phase armature currents are generated because of the saturated core with a low value of the induced EMF voltage [17], [46], [52]. The values of τ_p, excluding 0.66, increase or decrease the slot angle, producing a high-rated current and copper loss as a result of the magnetic loading of the core material. This considerably reduces the efficiency and PF, as shown in Fig. 9.

B. PM POSITION (L_P)

The PM position (L_P) and slot angle (α_m) are correlated. For high efficiency and PF, an optimized value of distance (L_P) corresponding to the slot angle (α_m) needs to be determined. The influence of this distance (L_P) on the performance characteristics is shown in Fig. 10. Similarly, L_P (33 mm) yields the appropriate back EMF at a fixed slot angle of 149° with

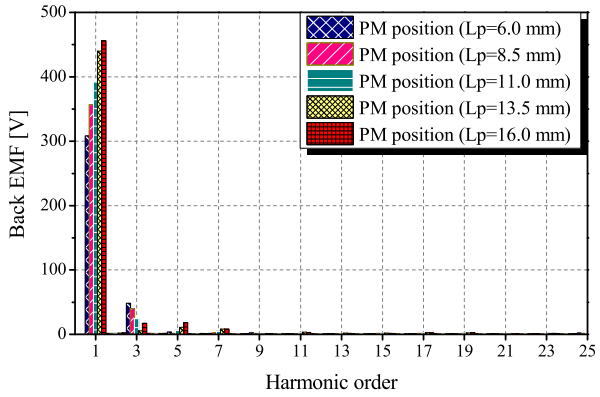

FIGURE 10. Back EMF harmonic analysis at different PM positions (L_P).

low third-, fifth- and seventh- harmonic components, as compared to a PM position of 35.5 mm (Fig. 10). When the slot angle is fixed to its optimum value (i.e., 149°) and the distance (L_P) is further decreased or increased besides the fixed value (33 mm), then the gap between the rotor bars and PM slots is decreased and reaches a minimum value at point P_1 or P_2, as shown in Fig. 5. The low value of L_P will result in additional PM-to-PM flux leakage as well as flux leakage through the flux barriers and the *Rib*. The effective air-gap flux density and flux linkage will be altered, and the low induced voltage will have a negative impact on the performance of the LSPM machine. If L_P (e.g., 33 m) is increased further to a fixed value of the slot angle (149°), the cage bars will penetrate the PM, and the flux barrier slots and the rotor will be destroyed mechanically under high-speed operation (n_r). Therefore, the distance L_P at an optimal value of the slot angle (α_m) is an indispensable parameter in the rotor design of the LSPM motor, for achieving high mechanical strength.

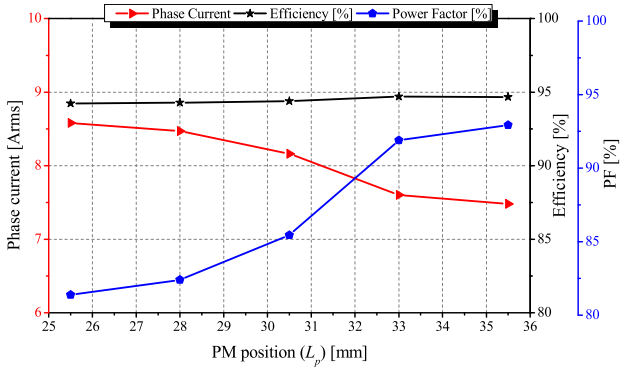

FIGURE 11. Steady-state analysis at different PM positions (L_P).

At a low value of L_P, the efficiency and PF have poor characteristics as a result of the additional PM-to-PM flux leakage as well as the flux leakage through the *Rib*. Consequently, a high armature current with increased copper loss is generated, as shown in Fig. 11 and Table 5. A slot angle of 152° and a distance of 35.5 mm were not chosen because, at these values of the slot angle and L_P, the gap between

TABLE 5. Performance characteristics of the 7.5-kW LSPM motor.

Output	Items							
	Slot angle (α_m) [°]				PM position (L_P) [mm]			
	140	143	146	149	25.5	28	30.5	33
Back EMF [V_{rms}]	214.9	232.3	275.7	302.3	228.1	255.8	284.4	302.3
Rated current [A_{rms}]	10.1	9.26	8.30	7.60	8.58	8.35	8.14	7.60
Efficiency [%]	93.4	93.9	94.3	94.7	94.2	94.3	94.4	94.7
PF [%]	69.8	75.7	84.1	91.9	81.4	82.4	85.4	91.9
Ripple factor [%]	33.1	27.8	21.3	12.4	23.1	18.9	17.5	12.4
Copper loss [W]	249.1	209.4	168.2	139.6	179.8	170.3	161.8	139.6

the slot and the rotor bar is <1.5 mm at points P_1 and P_2, which is the minimum required gap length for the mechanical construction of the LSPM rotor under high-speed operation. Therefore, in this prototype LSPM motor, to meet the required specifications, the optimal values for slot angle (α_m), distance (L_P), and *Rib* are 149°, 33 mm, and 4.805 mm, respectively. Furthermore, these optimal values of slot angle (149°) and distance L_P (33 mm) satisfy the mechanical constraints for rotor construction. The gap lengths between the slot and the rotor bar at points P_1 and P_2 are 1.785 mm and 1.523 mm, respectively, both of which are >1.5 mm.

Considering the correlation between back EMF and efficiency, the objective function is set to magnify the back EMF voltage. Meanwhile, both design variables (152° and 35.5 mm) yield a high value of the fundamental component of induced EMF voltage. This could also undermine the starting torque as the braking torque is proportional to the square of the induced EMF [1], [6], [7]. These design constraints should be considered when accounting for the back EMF voltage, because the values of the slot angle (152°) and distance (35.5 mm) can have a negative impact on the LSPM start-up (high starting current) and synchronization performance. The performance characteristics of the 7.5kW LSPM motor at various slot angles (α_m) and PM positions (L_P) are summarized in Table 5. The optimized values of slot angle (149°) and L_P (33 mm) produce low higher-order harmonics and also reduce the braking as well as the pulsating torque caused by the interaction between the stator current and the induced EMF harmonics. Hence, to minimize the cogging torque for a low starting current, the high-order harmonics of the back EMF should be reduced as much as possible, during the motor design process [3], [5], [7].

C. INDUCTANCE SALIENCY RATIO (ξ)

The inductance design estimates the major behavior of the electrical machine. Hence, the precise computation of the *dq*-axis inductances are necessary. The design variables are

chosen to optimize the PM slot shape in the rotor core and also to enhance the steady-state performance of the LSPM by optimizing the saliency ratio [6], [8], [40]. The ratio of inductance difference between the magnetic paths of the d-axis (L_d) and q-axis (L_q) is the saliency ratio, used to improve the output of the objective function. The proposed rotor structure of the LSPM motor (Fig. 1) with features identical to the conventional IPM motor, has inserted magnets in the d axis causes $L_q > L_d$, because of the variation in the magnetic resistance between the d-axis and q-axis [2], [6], [52]. In IPM-type LSPM motor, the armature current amplitude has a great impact on the dq-axis inductances. The q-axis inductance change significantly with the increase of current amplitude because of the variation in core saturation and cross coupling effect [9], [42], [53]. The FEM analysis is used to calculate the inductance variation based on the rotor geometry with the change of current amplitude, as shown in Fig. 12 [52].

At different slot angles, the flux path along the d-axis remains the same; however, the q-axis flux path varies every time the slot angle changes. Therefore, only the influence of slot angles (α_m) on the d-axis and q-axis inductance are investigated. This results in greater differences in the magnetic resistance of the dq-axes. The greater the difference between the d-axis and q-axis inductances, the higher is the saliency ratio; however, this ratio cannot surpass the theoretical limitation because of the mechanical stress and the effect of field saturation [2], [8], [40], [52]. The saliency ratio (ξ) is expressed as

$$\xi = \frac{L_q}{L_d}, \tag{37}$$

where

$$L_d = \frac{\psi_o \cos\alpha - \psi_a}{i_d}, \tag{38}$$

$$L_q = \frac{\psi_o \sin\alpha}{i_q}, \tag{39}$$

$i_d = -I_a \sin\gamma$, $i_q = I_a \cos\gamma$, ψ_a is the no-load flux linkage, ψ_o is the flux linkage at the rated input current, α is the phase difference angle between flux linkages at no-load to full-load conditions, I_a is peak input current, and γ is the current vector angle [45].

In this LSPM rotor structure, the saliency ratio is improved by adding a rectangular magnet in the flux path of the d-axis and several flux barriers. The FEM is used to compute the d-axis and q-axis inductances under varying load conditions based on different slot angles (α_m) are shown in Fig. 12 [10], [52]. As the slot angle increases, the magnet and shaft volume are reduced. Therefore, the area between the magnet slot and the conductor bar is secured, resulting in a lower reluctance for the q axis and a large value of L_q. The size and trend of L_d did not vary significantly with the change in the slot angles of the side PM segment. The optimized saliency ratio at different slot angles increases the PF as shown in Fig. 13 as well as improves the starting performance [6], [45] of the LSPM motor significantly. The influence of magnetic saturation on the inductance is not constant

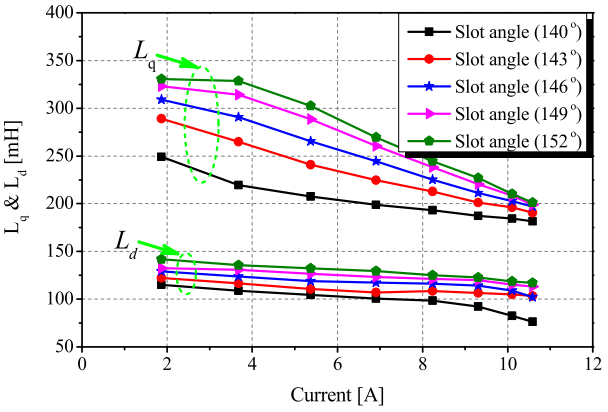

FIGURE 12. d- and q-axis inductance calculations for the LSPM motor at different slot angles (α_m).

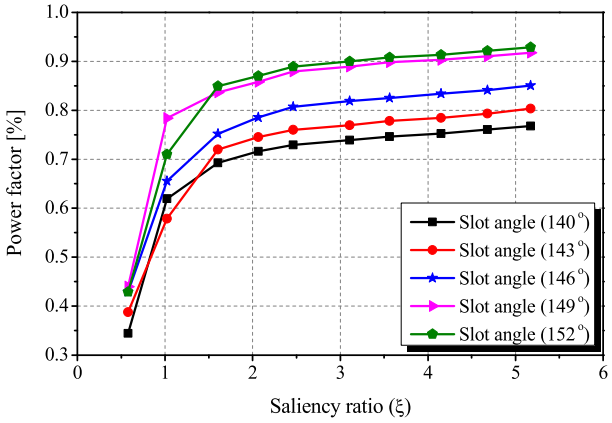

FIGURE 13. Effects of inductance saliency ratio on the power factor of LSPM motor at different slot angles (α_m).

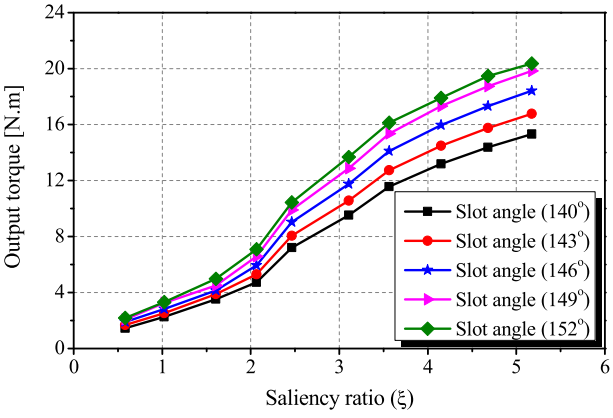

FIGURE 14. Effects of inductance saliency ratio on the output torque of LSPM motor at different slot angles (α_m).

but change with d-q axis current. Therefore, when armature current is enhanced, the magnetic saturation of the q-axis is increased causing a high reluctance path for the flux due to armature reaction of q-axis magnetic circuit and decreases the L_q inductance as well as saliency ratio [52], [53]. The impact of the dq-axis inductances on the output torque performance at different slot angles is shown in Fig. 14. At low saliency

ratio, the output torque produced by the prototype LSPM motor is very small due to high magnetic saturation of the core material under extreme loading conditions. Consequently, the values of the efficiency and PF of the LSPM motor at a rated torque of 19.9 Nm are 94.7% and 91.9%, respectively.

With the increase of input current applied to armature winding, the strong cross magnetization and core saturation causes low value of the dq-axis inductances, and deliver poor PF and output torque as given in Figs. 13 and 14 [42], [52]. Low inductance values for slot angles (140°, 143°, and 146°) result in a strong cross magnetization through the *Rib* and operate at high stator currents. This causes greater saturation of the core material. The core saturation relies on the current in the same axis as well as that in the orthogonal axis [9], [42]. A lower slot angle (140°, 143°, and 146°) reduces the spare area (*Rib*), increases the (PM-to-PM) flux leakage, and increases the saturation along the q axis, which negatively impacts the inductance design. With an increase in the magnetic saturation along the q axis, L_q starts to decrease, and the reluctance torque, which is proportional to $(L_q - L_d)$, is also reduced. This leads to a reduction in the total electromagnetic torque (T_e) and also causes greater amounts of phase current to be drawn through the armature winding, thereby increasing copper losses [42], [52], [53].

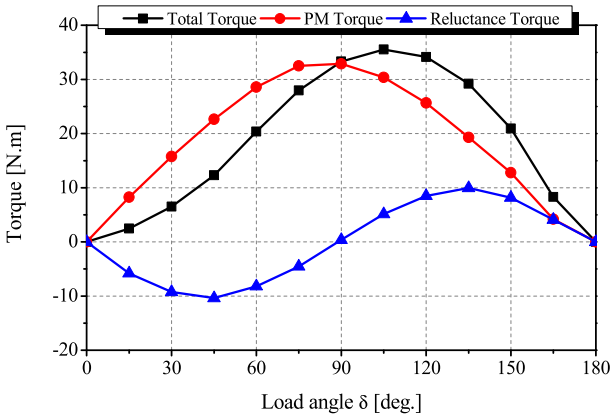

FIGURE 15. Calculation of different torque components of LSPM with the change of load angle (δ).

D. TORQUE PERFORMANCE

The magnetic anisotropy (i.e., reactance) between quadrature and direct axis produces reluctance torque due to the presence of a magnet in the LSPM rotor. The saliency ratio improves the reluctance torque component, which varies as a function of the inductances variance, and assists in enhancing the total electromagnetic torque (T_e) under the steady-state condition as given in Fig. 15 [3], [8]. The improved saliency ratio helps to reduce the amount of high-cost magnetic material required to produce the necessary output torque. This reduction in the magnetic material decreases PM torque. The reduction of magnetic torque is compensated with the improved reluctance torque component by using the optimal electromagnetic design consideration of the LSPM rotor [53].

The optimized values of the design variables are selected (149° and 33 mm) for the dynamic analysis of the LSPM motor, to evaluate the influence of torque components on the torque capability with their average values are plotted against the load angle (δ), given in Fig. 15. The total electromagnetic torque generated by the LSPM is expressed as

$$T_e = \frac{3}{2}\frac{P}{2}\left(\lambda_{PM} i_q - (\xi - 1) L_d i_d i_q\right), \tag{40}$$

where λ_{PM} is the magnetic flux linkage to the stator three-phase winding. An examination of (40) shows that the total torque involves two components:

$$T_e = T_{PM} + T_{rel} \tag{41}$$

The first term, referred to as the PM torque (T_{PM}), is obtained through the interaction between the stator q-axis current and the rotor magnet. The presence of magnets in the rotor d-axis produces the second term, which is known as the reluctance torque (T_{rel}), because of the difference in their magnetic resistance. The sum of the magnetic and reluctance torques yields the total torque and the load angle (δ) required to achieve the peak value of the total electromagnetic torque at an electrical degree exceeding 90°, as shown in Fig. 15. The reluctance torque component causes this shift in the load angle. The reluctance torque increases the PM torque in the load angle region between 90° E and 180° E and decreases it between 0° E and 90° E. The loci of the load angle against the maximum output torque based on the armature current amplitude is used to calculate the optimal torque per unit stator current operation of the machine [45].

From the PF and torque equations, it is evident that the variations in d-axis and q-axis inductances play a critical role in enhancing the performance of the synchronous machine. Another important design variable is the *Rib* used for the performance improvement of the LSPM motor. A smaller *Rib* causes a high PM torque as the result of the reduced magnetic flux leakage. In contrast, a larger *Rib* causes greater flux leakage and decreases the magnetic torque. Therefore, optimization of the geometric parameters of a rotor is an important design criterion to reduce the flux leakage and achieve enhanced inductance saliency ratio and torque capability [8], [42], [52]. The lumped magnetic equivalent parameters are imperative in optimizing the air-gap flux density and the inductance design to achieve the required design specifications of the LSPM motor, with a minimum rated current to ensure reduced core and copper losses.

V. DEMAGNETIZATION ANALYSIS OF THE PROTOTYPE LSPM MOTOR

Magnets composed of rare-earth materials (Nd–Fe–B) offer excellent magnetic characteristics owing to their high remanent flux density (B_r) and coercive force (H_c). Hence, an optimized slot shape of the PM is a critical design parameter to avoid demagnetization of the magnets under the influence of high reversed magnetic field at different temperatures. Thus, the rotor bars used in IM are redesigned to reduce

the high starting current of the LSPM motor and minimize the demagnetization effects if the high armature current produces a magnetic field in the direction opposite to the rotor d-axis [45], [46], [54].

The segmented magnets under the squirrel-cage rotor help to enhance the torque segregation and robustness against demagnetization, by inducing high eddy currents in the rotor bar during asynchronous operation in order to protect the PM against the MMF at high temperatures [2], [46]. As sensors or encoders are not used to determine the initial rotor position in the LSPM motor in order to avoid the magnet demagnetization, the worst initial position is determined by calculating the highest starting current value under different load angles. The demagnetization analysis is performed using FEM for the prototype LSPM motor by applying an external demagnetizing field calculated on the basis of the worst initial positions at different temperatures, as shown in Fig. 16.

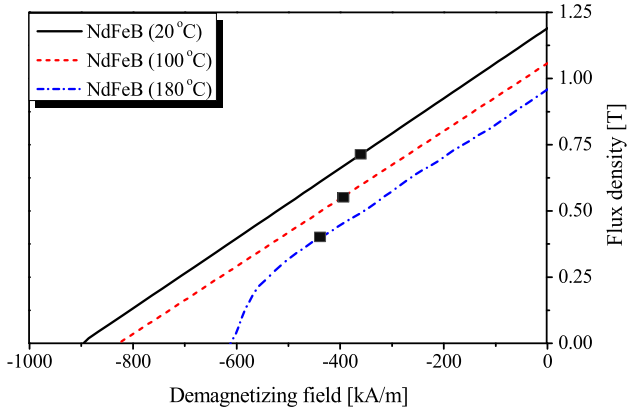

FIGURE 16. Demagnetization analysis of LSPM based on temperatures.

However, to perform the demagnetization analysis, the d-axis of the armature magnetic circuit and rotor are fixed against each other in the static condition [43], [45]. The nonlinear characteristics of the magnets and core are also considered to perform the static demagnetization analysis, as shown in Fig. 16 [9]. This figure (Fig. 16) indicates the operating point of the PM on the B–H curve at different temperatures obtained by applying a demagnetizing current $(-i_d)$ to the armature coil to generate the reverse magnetic field. The impact of the applied reverse magnetomotive force (MMF) is calculated by analyzing the directions of the magnetic field vectors of the PM. If magnetic field vectors of the PM become opposite under the influence of a high armature reaction field (MMF), then demagnetization of the magnet will occur. It means PM has a flux density lower than the knee point value [9], [43], [46].

Under transient-state conditions, the short-circuit current generated by the induced voltage in the rotor bars produces a magnetic field that is opposite to the armature field; this limits the impact of the reverse magnetic field acting on the PM, thereby preventing demagnetization during high starting current operation [3], [45]. These eddy currents may also

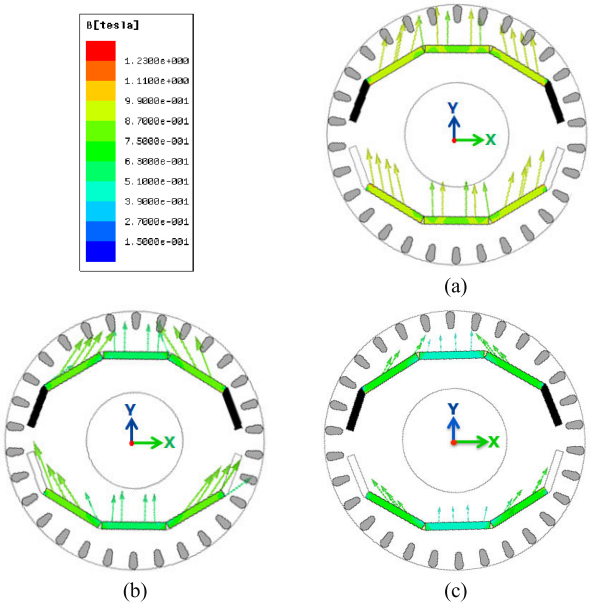

FIGURE 17. Magnetic flux density vectors of the PM under armature reaction at (a) 20 °C, (b) 100 °C, and (c) 180 °C.

enhance the rotor core losses. The knee point value of an N35EH magnet at 180 °C is 0.15 T. Therefore, the marked range of the magnetic flux density for an N35EH magnet during a demagnetization analysis under the worst operating condition is 0.15–1.23 T, as shown in Fig. 17(a). Figure 17 presents the flux density vectors of the PM under an armature reaction field at different operating temperatures. The maximum values of the demagnetizing currents $(-i_d)$ given to armature coils at 20 °C, 100 °C, and 180 °C are 193.7 A_{peak}, 178.2 A_{peak}, and 164.8 A_{peak}, respectively. Thus, the magnets inside the rotor iron core are protected from the armature winding MMF and the field harmonics in the air gap produced by stator slots that result in electromagnetic vibrations and noise [44], [54].

VI. CONCLUSION

In this article, to satisfy the required design specifications, an analytical model based on a linear saturated lumped parametric model was developed, in order to provide solutions within a short period. The viability of the prototype LSPM model based on various design variables was verified through FEM. A novel optimized rotor structure was developed, and mathematical expressions are derived using the proposed analytical model. This structure achieved improved no-load performance as well as an enhanced saliency ratio. The differences between the d-axis and q-axis inductances could be exploited to effectively increase the PF and efficiency of the LSPM motor.

The improved rotor structure generated a reasonable reluctance torque with a low-rated current (7.60 A_{rms}) and torque ripples, thereby reducing the core loss; this has a significant impact on the synchronous torque capability of the LSPM motor. A demagnetization analysis based on temperature was

used to certify the robustness of the designed rotor shape against demagnetization, even under the worst operating condition (at 180 °C). The results of this study indicate that careful selections of the magnet slot angle (α_m) and position (L_P) with respect to the magnetic flux barriers play an important role in the steady-state characteristics and also improve the possible design of the PM rotor, while satisfying mechanical structural constraints. Hence, using the optimal values of the design parameters, the desired air-gap flux density as well as back EMF were achieved, and a 7.5-kW two-pole, three-phase prototype LSPM model was developed.

REFERENCES

[1] M. Lin, D. Li, Y. Zhao, X. Ren, and R. Qu, "Improvement of starting performance for line-start permanent magnet motors by winding reconfiguration," *IEEE Trans. Ind. Appl.*, vol. 56, no. 3, pp. 2441–2450, May 2020.

[2] K. Kurihara and M. A. Rahman, "High-efficiency line-start interior permanent-magnet synchronous motors," *IEEE Trans. Ind. Appl.*, vol. 40, no. 3, pp. 789–796, May 2004.

[3] R. T. Ugale and B. N. Chaudhari, "Rotor configurations for improved starting and synchronous performance of line start permanent-magnet synchronous motor," *IEEE Trans. Ind. Electron.*, vol. 64, no. 1, pp. 138–148, Jan. 2017.

[4] L. S. Maraaba, Z. M. Al-Hamouz, A. S. Milhem, and M. A. Abido, "Neural network-based diagnostic tool for detecting stator inter-turn faults in line start permanent magnet synchronous motors," *IEEE Access*, vol. 7, pp. 89014–89025, Jun. 2019.

[5] T. Marcic, B. Stumberger, and G. Stumberger, "Comparison of induction motor and line-start IPM synchronous motor performance in a variable-speed drive," *IEEE Trans. Ind. Appl.*, vol. 48, no. 6, pp. 2341–2352, Nov. 2012.

[6] A. Hassanpour Isfahani and S. Vaez-Zadeh, "Effects of magnetizing inductance on start-up and synchronization of line-start permanent-magnet synchronous motors," *IEEE Trans. Magn.*, vol. 47, no. 4, pp. 823–829, Apr. 2011.

[7] M. M. Ghahfarokhi, A. D. Aliabad, S. T. Boroujeni, E. Amiri, and V. Z. Faradonbeh, "Analytical modelling and optimisation of line start LSPM synchronous motors," *IET Electr. Power Appl.*, vol. 14, no. 3, pp. 398–408, Mar. 2020.

[8] G.-H. Kang, B.-K. Lee, H. Nam, J. Hur, and J.-P. Hong, "Analysis of single-phase line-start permanent-magnet motor considering iron loss and parameter variation with load angle," *IEEE Trans. Ind. Appl.*, vol. 40, no. 3, pp. 797–805, May 2004.

[9] G.-H. Kang, J. Hur, H. Nam, J.-P. Hong, and G.-T. Kim, "Analysis of irreversible magnet demagnetization in line-start motors based on the finite-element method," *IEEE Trans. Magn.*, vol. 39, no. 3, pp. 1488–1491, May 2003.

[10] H. Mirahki and M. Moallem, "Torque calculation in interior permanent magnet synchronous machine using improved lumped parameter models," *Prog. Electromagn. Res. M*, vol. 39, pp. 131–139, Oct. 2014.

[11] L. Zhu, S. Z. Jiang, Z. Q. Zhu, and C. C. Chan, "Analytical modeling of open-circuit air-gap field distributions in multisegment and multilayer interior permanent-magnet machines," *IEEE Trans. Magn.*, vol. 45, no. 8, pp. 3121–3130, Aug. 2009.

[12] E. C. Lovelace, T. M. Jahns, and J. H. Lang, "A saturating lumped-parameter model for an interior PM synchronous machine," *IEEE Trans. Ind. Appl.*, vol. 38, no. 3, pp. 645–650, May 2002.

[13] S. Oh, S. Min, and J.-P. Hong, "Air gap flux density waveform design of surface-mounted permanent magnet motor considering magnet shape and magnetization direction," *IEEE Trans. Magn.*, vol. 49, no. 5, pp. 2393–2396, May 2013.

[14] K. I. Laskaris and A. G. Kladas, "Permanent-magnet shape optimization effects on synchronous motor performance," *IEEE Trans. Ind. Electron.*, vol. 58, no. 9, pp. 3776–3783, Sep. 2011.

[15] D.-K. Lim, K.-P. Yi, D.-K. Woo, H.-K. Yeo, J.-S. Ro, C.-G. Lee, and H.-K. Jung, "Analysis and design of a multi-layered and multi-segmented interior permanent magnet motor by using an analytic method," *IEEE Trans. Magn.*, vol. 50, no. 6, pp. 1–8, Jun. 2014.

[16] Y. Chen, Z. Q. Zhu, and D. Howe, "Three-dimensional lumped-parameter magnetic circuit analysis of single-phase flux-switching permanent-magnet motor," *IEEE Trans. Ind. Appl.*, vol. 44, no. 6, pp. 1701–1710, 2008.

[17] D.-K. Lim and J.-S. Ro, "Analysis and design of a delta-type interior permanent magnet synchronous generator by using an analytic method," *IEEE Access*, vol. 7, pp. 85139–85145, Jul. 2019.

[18] Y. Kano, T. Kosaka, and N. Matsui, "A simple nonlinear magnetic analysis for axial-flux permanent-magnet machines," *IEEE Trans. Ind. Electron.*, vol. 57, no. 6, pp. 2124–2133, Jun. 2010.

[19] G. De Donato, F. G. Capponi, and F. Caricchi, "No-load performance of axial flux permanent magnet machines mounting magnetic wedges," *IEEE Trans. Ind. Electron.*, vol. 59, no. 10, pp. 3768–3779, Oct. 2012.

[20] A. Parviainen, M. Niemela, and J. Pyrhönen, "Modeling of axial flux permanent-magnet machines," *IEEE Trans. Ind. Appl.*, vol. 40, no. 5, pp. 1333–1340, Sep. 2004.

[21] Z. Q. Zhu, Y. Pang, D. Howe, S. Iwasaki, R. Deodhar, and A. Pride, "Analysis of electromagnetic performance of flux-switching permanent-magnet machines by nonlinear adaptive lumped parameter magnetic circuit model," *IEEE Trans. Magn.*, vol. 41, no. 11, pp. 4277–4287, Nov. 2005.

[22] M. L. Bash and S. D. Pekarek, "Modeling of salient-pole wound-rotor synchronous machines for population-based design," *IEEE Trans. Energy Convers.*, vol. 26, no. 2, pp. 381–392, Jun. 2011.

[23] M. Cheng, K. T. Chau, C. C. Chan, E. Zhou, and X. Huang, "Nonlinear varying-network magnetic circuit analysis for doubly salient permanent-magnet motors," *IEEE Trans. Magn.*, vol. 36, no. 1, pp. 339–348, Jan. 2000.

[24] M. Cheng, K. T. Chau, and C. C. Chan, "Design and analysis of a new doubly salient permanent magnet motor," *IEEE Trans. Magn.*, vol. 37, no. 4, pp. 3012–3020, Jul. 2001.

[25] Q. Chen, G. Liu, W. Zhao, and M. Shao, "Nonlinear adaptive lumped parameter magnetic circuit analysis for spoke-type fault-tolerant permanent-magnet motors," *IEEE Trans. Magn.*, vol. 49, no. 9, pp. 5150–5157, Sep. 2013.

[26] J. Li, K. Wang, and H. Zhang, "Comparative analysis of spoke-type, consequent-pole and hybrid-pole permanent magnet machines," *IET Electric Power Appl.*, vol. 14, no. 4, pp. 648–657, Apr. 2020.

[27] A. R. Tariq, C. E. Nino-Baron, and E. G. Strangas, "Iron and magnet losses and torque calculation of interior permanent magnet synchronous machines using magnetic equivalent circuit," *IEEE Trans. Magn.*, vol. 46, no. 12, pp. 4073–4080, Dec. 2010.

[28] P. Liang, Y. Pei, F. Chai, and K. Zhao, "Analytical calculation of d-and q-axis inductance for interior permanent magnet motors based on winding function theory," *Energies*, vol. 9, no. 8, p. 580, Jul. 2016.

[29] W. Kemmetmüller, D. Faustner, and A. Kugi, "Modeling of a permanent magnet synchronous machine with internal magnets using magnetic equivalent circuits," *IEEE Trans. Magn.*, vol. 50, no. 6, pp. 1–14, Jun. 2014.

[30] Z. Zhang, C. Xia, Y. Yan, Q. Geng, and T. Shi, "A hybrid analytical model for open-circuit field calculation of multilayer interior permanent magnet machines," *J. Magn. Magn. Mater.*, vol. 435, pp. 136–145, Aug. 2017.

[31] Z. Q. Zhu, D. Howe, and C. C. Chan, "Improved analytical model for predicting the magnetic field distribution in brushless permanent-magnet machines," *IEEE Trans. Magn.*, vol. 38, no. 1, pp. 229–238, Jan. 2002.

[32] D.-K. Lim, S.-Y. Jung, K.-P. Yi, and H.-K. Jung, "A novel sequential-stage optimization strategy for an interior permanent magnet synchronous generator design," *IEEE Trans. Ind. Electron.*, vol. 65, no. 2, pp. 1781–1790, Feb. 2018.

[33] D. Zarko, D. Ban, and T. A. Lipo, "Analytical calculation of magnetic field distribution in the slotted air gap of a surface permanent-magnet motor using complex relative air-gap permeance," *IEEE Trans. Magn.*, vol. 42, no. 7, pp. 1828–1837, Jul. 2006.

[34] Z. Q. Zhu and D. Howe, "Instantaneous magnetic field distribution in brushless permanent magnet DC motors. III. Effect of stator slotting," *IEEE Trans. Magn.*, vol. 29, no. 1, pp. 143–151, Jan. 1993.

[35] D. Zarko, D. Ban, and T. A. Lipo, "Analytical solution for cogging torque in surface permanent-magnet motors using conformal mapping," *IEEE Trans. Magn.*, vol. 44, no. 1, pp. 52–65, Jan. 2008.

[36] L. Fang, S.-O. Kwon, and J.-P. Hong, "Conformal transformation technique for prediction of the magnetic field distribution in an IPM motor," in *Proc. Int. Conf. Electr. Mach. Syst.*, vol. 3, 2005, pp. 2124–2128.

[37] X. Lu, K. L. V. Iyer, K. Mukherjee, and N. C. Kar, "Development of a novel magnetic circuit model for design of premium efficiency three-phase line start permanent magnet machines with improved starting performance," *IEEE Trans. Magn.*, vol. 49, no. 7, pp. 3965–3968, Jul. 2013.

[38] A. Ghaffari, A. Rahideh, H. Ghaffari, A. Vahaj, and A. Mahmoudi, "Comparison between 2-D and 0-D analytical models for slotless double-sided inner armature linear permanent magnet synchronous machines," *Int. Trans. Electr. Energ. Syst.*, vol. 30, May 2020, Art. no. e12509.
[39] C.-C. Hwang and Y. H. Cho, "Effects of leakage flux on magnetic fields of interior permanent magnet synchronous motors," *IEEE Trans. Magn.*, vol. 37, no. 4, pp. 3021–3024, Jul. 2001.
[40] E. C. F. Lovelace, "Optimization of a magnetically saturable interior permanent-magnet synchronous machine drive," Massachusetts Inst. Technol., Cambridge, MA, USA, Tech. Rep., 2000.
[41] C. Mi, M. Filippa, W. Liu, and R. Ma, "Analytical method for predicting the air-gap flux of interior-type permanent-magnet machines," *IEEE Trans. Magn.*, vol. 40, no. 1, pp. 50–58, Jan. 2004.
[42] B. Stumberger, G. Stumberger, D. Dolinar, A. Hamler, and M. Trlep, "Evaluation of saturation and cross-magnetization effects in interior permanent-magnet synchronous motor," *IEEE Trans. Ind. Appl.*, vol. 39, no. 5, pp. 1264–1271, Sep. 2003.
[43] J. Hong, S. Park, D. Hyun, T.-J. Kang, S. B. Lee, C. Kral, and A. Haumer, "Detection and classification of rotor demagnetization and eccentricity faults for PM synchronous motors," *IEEE Trans. Ind. Appl.*, vol. 48, no. 3, pp. 923–932, May 2012.
[44] C. Debruyne, M. Polikarpova, S. Derammelaere, P. Sergeant, J. Pyrhonen, J. J. M. Desmet, and L. Vandevelde, "Evaluation of the efficiency of line-start permanent-magnet machines as a function of the operating temperature," *IEEE Trans. Ind. Electron.*, vol. 61, no. 8, pp. 4443–4454, Aug. 2014.
[45] J. R. Hendershot and T. J. E. Miller, *Design of Brushless Permanent-Magnet Machines*, 2nd ed. Venice, FL, USA: Motor Design Books, 2010.
[46] M. J. Melfi, S. D. Umans, and J. E. Atem, "Viability of highly efficient multi-horsepower line-start permanent-magnet motors," *IEEE Trans. Ind. Appl.*, vol. 51, no. 1, pp. 120–128, Jan. 2015.
[47] G. Liu, M. Shao, W. Zhao, J. Ji, Q. Chen, and Q. Feng, "Modeling and analysis of Halbach magnetized permanent-magnets machine by using lumped parameter magnetic circuit method," *Prog. Electromagn. Res. M*, vol. 41, pp. 177–188, Mar. 2015.
[48] A. Rahideh and T. Korakianitis, "Analytical magnetic field distribution of slotless brushless PM motors. Part 2: Open-circuit field and torque calculations," *IET Electr. Power Appl.*, vol. 6, no. 9, pp. 639–651, Nov. 2012.
[49] X. Liu, J. Gao, S. Huang, and K. Lu, "Magnetic field and thrust analysis of the U-channel air-core permanent magnet linear synchronous motor," *IEEE Trans. Magn.*, vol. 53, no. 6, pp. 1–4, Jun. 2017.
[50] A. Rahideh, A. Ghaffari, A. Barzegar, and A. Mahmoudi, "Analytical model of slotless brushless PM linear motors considering different magnetization patterns," *IEEE Trans. Energy Convers.*, vol. 33, no. 4, pp. 1797–1804, Dec. 2018.
[51] K. Kurihara, G. Wakui, and T. Kubota, "Steady-state performance analysis of permanent magnet synchronous motors including space harmonics," *IEEE Trans. Magn.*, vol. 30, no. 3, pp. 1306–1315, May 1994.
[52] X. Liu, H. Chen, J. Zhao, and A. Belahcen, "Research on the performances and parameters of interior PMSM used for electric vehicles," *IEEE Trans. Ind. Electron.*, vol. 63, no. 6, pp. 3533–3545, Jun. 2016.
[53] W. Q. Chu and Z. Q. Zhu, "Average torque separation in permanent magnet synchronous machines using frozen permeability," *IEEE Trans. Magn.*, vol. 49, no. 3, pp. 1202–1210, Mar. 2013.
[54] J.-X. Shen, P. Li, M.-J. Jin, and G. Yang, "Investigation and countermeasures for demagnetization in line start permanent magnet synchronous motors," *IEEE Trans. Magn.*, vol. 49, no. 7, pp. 4068–4071, Jul. 2013.

ABDUL WAHEED received the B.S. degree in electrical engineering (electronics) from The University of Faisalabad (TUF), Faisalabad, Pakistan, in 2012, and the M.S. degree in electrical engineering from Dong-A University (DAU), Busan, South Korea, in 2020. He is currently pursuing the Ph.D. degree with Chung-Ang University, Seoul, South Korea. His research interests include design and analysis of electrical machines, electric drives, and control.

JONG-SUK RO (Member, IEEE) received the B.S. degree in mechanical engineering from Hanyang University, Seoul, South Korea, in 2001, and the Ph.D. degree in electrical engineering from Seoul National University (SNU), Seoul, in 2008. He conducted research at the Research and Development Center, Samsung Electronics, as a Senior Engineer, from 2008 to 2012. From 2012 to 2013, he was a Postdoctoral Fellow with the Brain Korea 21 Information Technology, SNU. From 2013 to 2016, he was a BK Assistant Professor with the Brain Korea 21 Plus, SNU. He conducted research at the Electrical Energy Conversion System Research Division, Korea Electrical Engineering and Science Research Institute, as a Researcher, in 2013. In 2014, he was with the University of Bath, Bath, U.K. He is currently an Associate Professor with the School of Electrical and Electronics Engineering, Chung-Ang University, Seoul. His research interests include the analysis and optimal design of next-generation electrical machines.